Originally published as:

Key Points:
- Inversion of gravity, topography and seismic tomography data yields improved thermal, density and compositional models of the upper mantle
- Precambrian cratonic fragments were identified in Eastern Antarctica
- Almost undepleted lithosphere is found in the Lambert Graben and the Aurora Subglacial Basin

Supporting Information:
- Supporting Information S1
- Data Set S1

Correspondence to:
C. Haeger,
carina.haeger@gfz-potsdam.de

3-D Density, Thermal, and Compositional Model of the Antarctic Lithosphere and Implications for Its Evolution

C. Haeger[1,2] (iD), M. K. Kaban[1,3] (iD), M. Tesauro[4], A. G. Petrunin[1,3] (iD), and W. D. Mooney[5]

[1]GFZ German Research Centre for Geosciences, Potsdam, Germany, [2]Free University of Berlin, Berlin, Germany, [3]Schmidt Institute of Physics of the Earth, Moscow, Russia, [4]Dipartimento di Matematica e Geoscienze, Universita degli studi di Trieste, Trieste, Italy, [5]United States Geological Survey, Earthquake Science Center, Menlo Park, CA, USA

Abstract We create a 3-D density, temperature, and composition model of the Antarctic lithosphere using an integrative approach combining gravity, topography, and tomography data with mineral physics constraints and seismic data on crustal structures. The latter is used to create a new Moho and crustal density model. Temperature and thermal density variations are estimated based on *S* wave velocities from two independent tomography models (SL2013sv and AN1-S). Results of the Antarctic continent show the well-known distinction between East and West Antarctica in temperature and density to a depth of about 200 km. Incorporating compositional variations in the temperature calculations increases temperatures in depleted regions by up to 150 °C, giving improved insights into thermal structures. The thickness of the lithospheric root also varies strongly between these regions, with values below 100 km in the west and above 200 km in the east. Regions with negative compositional density variations (<-0.040 g/cm^3 at 100 km), high depletion (Mg # > 91.5), and low temperatures (<800 °C; central Dronning Maud Land, along the east flank of the Transantarctic Mountains) are interpreted as Precambrian cratonic fragments. Nearly undepleted lithosphere is found in the Lambert Graben and the Aurora Subglacial Basin and is attributed to Mesozoic rifting activity that has caused lithospheric rejuvenation.

Plain Language Summary Antarctica remains one of the least studied areas on Earth, because large ice masses and climate conditions strongly hinder measurements. It plays an important role in global phenomena such as sea level change. In order to understand and predict these processes, we need knowledge about the heat coming from the Earth's interior. It has been recently recognized that the thermal state of the lithosphere, the rigid outer shell of the Earth, plays an important role in controlling dynamics of the ice shield and, thus, global sea level changes. Therefore, we create a model of the lithosphere describing the variation in temperature, density, and composition. Before, such models were created by using some single data set (usually seismic tomography). We employ a new integrative approach, combining several data sets to create a comprehensive 3-D model of the Antarctic lithosphere. Combination of various data sets gives more robust models than when using a single approach. Our results of the Antarctic continent show strong differences between East and West Antarctica in temperature and density to a depth of about 200 km. Regions with negative compositional density variations and low temperatures are identified within East Antarctica and are interpreted as being substantially older than the surrounding continent.

1. Introduction

Density, temperature, and compositional variations in the uppermost mantle are important factors in determining the dynamics of the lithosphere. Therefore, in order to fully understand these dynamic processes, it is crucial to determine the location, magnitude, and origin of their heterogeneities. Also, as recently shown for Greenland, the heat flux from the lithosphere strongly affects ice dynamics (Petrunin, Rogozhina, et al., 2013). Hence, lithospheric temperature and heat flux estimates are important when modeling changes in the ice mass balance, glacial isostatic adjustment, and sea level changes caused by these processes. For Antarctica, our region of interest, information about the composition and temperature fields of the upper mantle is sparse. Geophysical in situ measurements are hindered by the logistical challenges presented by the thick ice sheet. Several studies estimate surface heat flux of Antarctica, including Maule et al. (2005) and Shapiro and Ritzwoller (2004) who used calculations of the thickness of the magnetic crust (Curie depth) and global surface wave tomography data, respectively. Later, An et al. (2015a) used their

tomography model and a similar mineral physics approach to estimate temperatures in the upper mantle, as well as surface heat flux, but without considering compositional variations. The results of these studies are very controversial. While Maule et al. (2005) predict comparably uniform heat flux throughout Antarctica with local maxima along the shoulder of the West Antarctic Rift System, and in Victoria Land, An et al. (2015a) and Shapiro and Ritzwoller (2004) find a clear distinction between East Antarctica (EANT) and West Antarctica (WANT) and attribute low heat flux to the shoulder of the West Antarctic Rift System. These studies differ strongly in the distribution of local variations and in amplitude, though, with Shapiro and Ritzwoller (2004) predicting much lower values and homogeneous variations in EANT. Radiogenic heat production is another important aspect to consider, when predicting heat flow. Yet high uncertainties are still linked to the distribution of radiogenic elements in the Antarctic crust (e.g., Burton-Johnson et al., 2017).

Even less is known about the compositional variations in the Antarctic upper mantle. Kuge and Fukao (2005) examined S and P velocity variations using broadband seismograms recorded at several stations within EANT and explained these with the presence of depleted continental lithosphere meaning high concentrations of olivine and a high magnesium number (Mg # = 100 Mg/(Mg + Fe)). On small scales, composition analysis has been conducted using xenolith data from rock exposure and glacier outlets (e.g., Goodge, 2018; Jacobs et al., 2015; Owada et al., 2013). Yet no continent-wide model of compositional variations exists to date for Antarctica.

Whereas existing thermal models of the Antarctic lithosphere have been calculated from a single type of data, such as satellite magnetics (Maule et al., 2005) or seismic tomography (An et al., 2015b; Shapiro & Ritzwoller, 2004), the joint analysis of several data sets can provide a more reliable model of temperature and compositional variations in the lithosphere (e.g., Ebbing et al., 2016; Kaban et al., 2015; Mooney & Kaban, 2010; Pappa et al., 2018). One effective method of analysis is the joint interpretation of seismic, gravity, and topographic data. Seismic velocity and density depend on temperature variations and composition of the upper mantle material but in fundamentally different ways (e.g., Cammarano et al., 2003; Stixrude & Lithgow-Bertelloni, 2005; Tesauro et al., 2014). This makes it possible to constrain both compositional and temperature variations within the lithosphere. Here we apply an integrative approach of Kaban et al. (2014) and Tesauro et al. (2014) to jointly analyze seismic tomography and gravity data to obtain a 3-D compositional, density, and temperature model of the Antarctic upper mantle. Since the choice of the tomography model may affect the calculated temperatures (e.g., Tesauro et al., 2014), we employ two independent tomography models (An et al., 2015b; Schaeffer & Lebedev, 2013) and compare the results obtained.

2. Tectonic Setting of Antarctica

About 99% of Antarctica is covered by an ice sheet that reaches a thickness maximum of 4,500 m (Figure 1b). Beneath the ice, the continent can be divided into EANT and WANT, two regions characterized by very different tectonics. While EANT is a stable Precambrian craton with a thick and relatively cold lithosphere, the lithosphere in WANT is thinner and hotter (Danesi & Morelli, 2001). WANT consists of several crustal microblocks that amalgamated in the Cenozoic and have undergone late-Cenozoic crustal extension (Dalziel & Elliot, 1982).

On smaller scales, both regions can be divided into subglacial orogens, basins, and rifts with the exact structure being under constant study (e.g., Ferraccioli et al., 2016). Figure 1a shows the bedrock topography with the names of the most relevant structures. The largest structure in EANT spans 0°–100°E and consists of a subglacial plateau that is interrupted by the Lambert Graben, a Mesozoic failed rift system that holds Antarctica's largest glacier, called Lambert Glacier (Harrowfield et al., 2005; Lisker et al., 2003; Powell et al., 1988). The highest elevations can be found in the Gamburtsev Subglacial Mountains (2,400 m) and Dronning Maud Land (2,500 m). The latter is a key region to understanding the amalgamation of Gondwana, because of its central location in the supercontinent. In the west, the Archean Grunehogna craton is bordered by the Mesoproterozoic Maud Belt. Adjacent to this craton, the Tonian Oceanic Arc Super Terrane represents juvenile Neoproterozoic remnants of the Mozambique Ocean (Jacobs et al., 2015). The southern margins of this region have still an enigmatic origin, but Jacobs et al. (2017) argue that it is bounded by a yet unidentified, possibly cratonic, tectonic feature. The most notable depressions within EANT are the Wilkes and the Aurora Subglacial Basins that lie up to 1 km below sea level. Recently, Chen et al. (2017) have
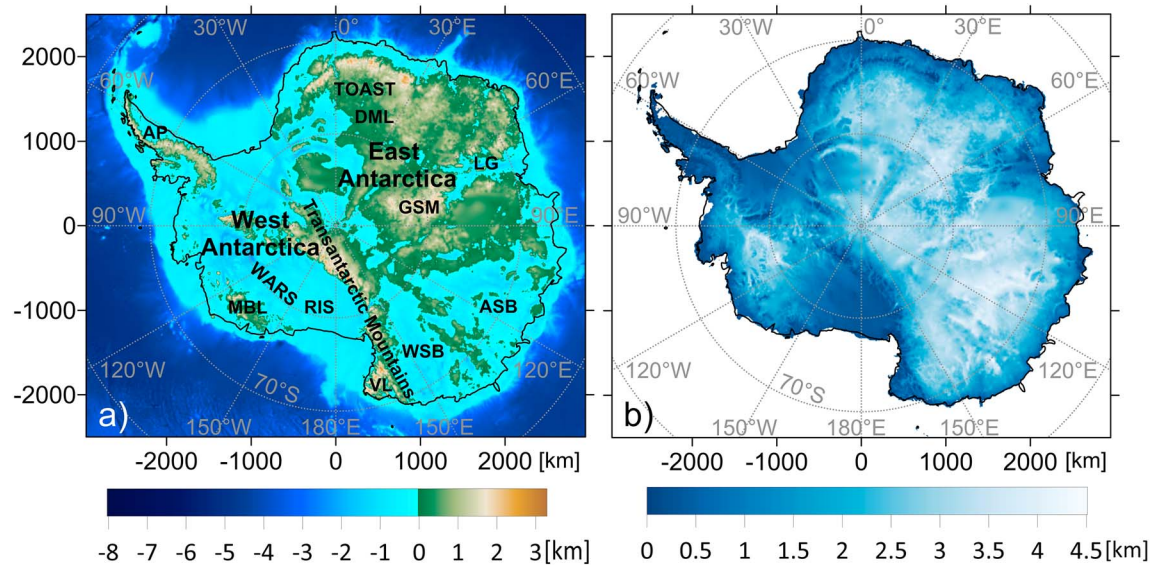
Figure 1. (a) Bedrock topography of Antarctica (Fretwell et al., 2013) and bathymetry of the surrounding ocean (Schaffer et al., 2014). Key tectonic units: AP = Antarctic Peninsula, ASB = Aurora Subglacial Basin, DML = Dronning Maud Land, GSM = Gamburtsev Subglacial Mountains, LG = Lambert Glacier, MBL = Marie Byrd Land, RIS = Ross Ice Shelf, TOAST = Tonian Oceanic Arc Super Terrane, VL = Victoria Land, WARS = West Antarctic Rift System, WSB = Wilkes Subglacial Basin. (b) Ice thickness (Fretwell et al., 2013).

shown that also the lithosphere of the East Antarctic shield is not as uniform as previously thought but is fragmented by the Lambert Graben.

Most of the West Antarctic lithospheric blocks are of Jurassic-Cretaceous age and moved independently prior to their amalgamation with EANT in the Cenozoic (Veevers, 2007). WANT is mostly characterized by sub-sea level bedrock topography with some areas of higher elevations like the Antarctic Peninsula or Marie Byrd Land, a region of intraplate volcanism (Hole & LeMasurier, 1994). Bordering Marie Byrd Land is the West Antarctic Rift System, a 750–1,000-km, largely aseismic rift system (O'Donnell & Nyblade, 2014) that had two distinct phases of extension: a prolonged period of diffuse extension in the Cretaceous and a period of extension focused in the Victoria Land Basin in the Paleogene (Huerta & Harry, 2007).

With a length of 3,500 m, a width of 200 km, and elevations of up to 4,500 m, the Transantarctic Mountains (TAM) are the largest noncontractional mountains in the world, meaning that the uplift was not caused by subduction or contraction (Morelli & Danesi, 2004; ten Brink & Stern, 1992) and mark the border of EANT and WANT. The tectonic process for their formation is debated and several uplift mechanisms have been proposed, including thermal uplift (e.g. Behrendt, 1999), mechanical uplift caused by a broken plate edge (e.g. ten Brink & Stern, 1992), or postrifting uplift (van Wijk et al., 2008).

3. Method

3.1. Modeling Concept

Since both composition and temperature variations can cause density variations, the distinction between these mechanisms has been the subject of multiple studies, both on the global (e.g., Deschamps et al., 2002; Simmons et al., 2009) and continental (e.g., Godey et al., 2004; Khan et al., 2013) scale. Many studies calculate thermal and compositional variations from seismic data alone, making the distinction difficult. To overcome this limitation, we apply a new technique developed by Kaban et al. (2014) that jointly inverts for seismic tomography, residual topography, and gravity data to simultaneously estimate temperature and composition in an iterative approach (Figure 2). We start by correcting the gravity field using available geophysical information, including topography, Moho depth, crustal densities, and deep density variations to obtain the residual mantle gravity field. Further, we correct the topography using the same fields to obtain the residual topography. Both fields are caused by subsurface density anomalies but respond to these
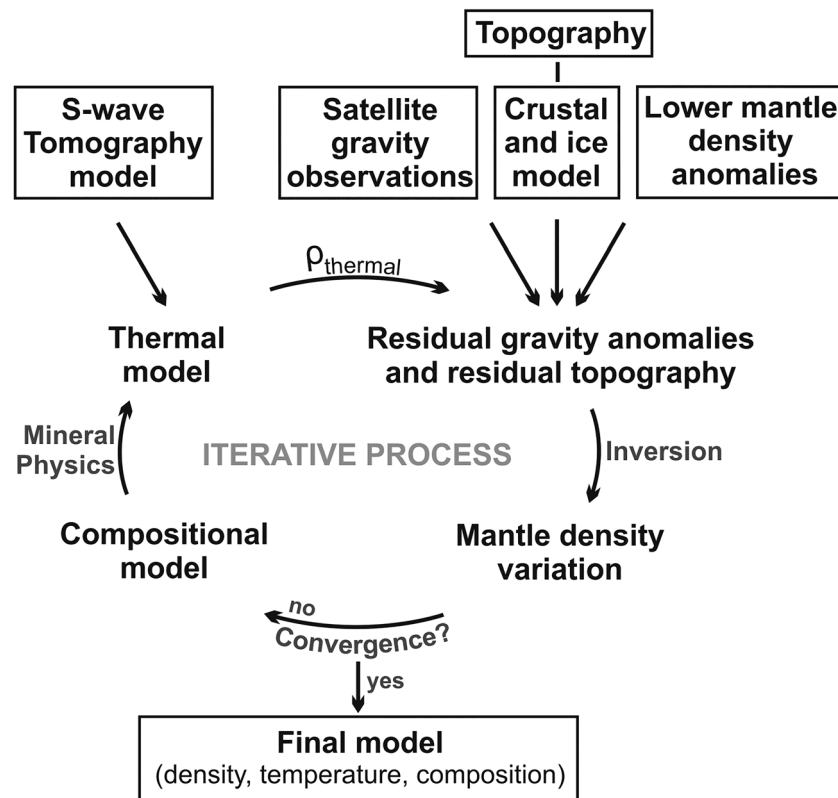
Figure 2. Schematic workflow of the iterative technique applied in this study.

anomalies in a fundamentally different way, thus allowing the inversion for density variations and their depths, more reliably than if only one observation was used. Using these density variations, new compositional models can be calculated. The initial thermal model was calculated using the mineral physics approach presented by Stixrude and Lithgow-Bertelloni (2005) assuming a uniform primitive mantle composition in the first step and then using the newly calculated composition model in the subsequent steps. Density variations related to the temperature variations are calculated and used to correct the density field for the next iteration. This scheme continues until the density changes between iterations are within 1% of the value and convergence is reached.

3.2. Thermal Modeling

To estimate temperature variations within the upper mantle, we calculate synthetic velocities taking into account anharmonic and anelastic properties. We assume a peridotite consisting of four mineral phases with an ideal solid solution of Mg and Fe end-member species with varying percentages: Olivine (Ol) with forsterite and fayalite, orthopyroxene (OPX) with enstatite and ferrosilite, clinopyroxene (CPX) with diopside and hedenbergite, and garnet (Gt) with pyrope and almandine. For Gt, a third Ca species (grossular) is considered to comprise a constant proportion of 20%. The mantle composition is varied between two end-members following Tesauro et al. (2014): A primitive mantle with Ol 58.5%, OPX 15%, CPX 11.5%, Gt 15%, and a magnesium number Mg # ($100 \times Mg/(Mg + Fe)$) of 89 and a depleted mantle with Ol 69.5%, OPX 21%, CPX 4%, Gt 5.5%, and Mg # 94. For the initial thermal model, a uniform primitive mantle composition is assumed.

In order to estimate synthetic shear wave velocities, the shear modulus and density for every mineral phase has to be calculated as a function of temperature and pressure using a mineral physics approach (Stixrude & Lithgow-Bertelloni, 2005). The parameters used for these calculations for each end-member mineral phase are taken from Cammarano et al. (2003) and Stixrude and Lithgow-Bertelloni (2005). For a given mantle composition, the shear modulus and density of the individual phases are averaged, and the anharmonic S wave velocity is calculated by

$$v_{s(\text{anh})} = \sqrt{\frac{\langle\mu\rangle}{\langle\rho\rangle}}. \tag{1}$$

Apart from the anharmonic effects, anelasticity also has to be estimated to determine synthetic velocities for varying temperature and pressure conditions. The synthetic S wave velocity can be described as (Cammarano et al., 2003)

$$v_{\text{syn}} = v_{s(\text{anh})}\left[1 - \frac{Q_s^{-1}}{2\tan\left(\frac{\pi a}{2}\right)}\right], \tag{2}$$

where Q_s is the S wave quality factor and a defines the frequency dependence of the attenuation. These factors describe anelasticity. The values for a as well as those necessary to calculate Q_s are taken from model Q4 from Cammarano et al. (2003). In order to finally estimate temperature variations from the input tomography models, we calculate synthetic velocity for distinct temperatures between 25 and 1,800 °C with a 5 °C spacing and for pressures corresponding to the depths for which the seismic tomography velocities (v_{meas}) have been estimated. Thus, we determine T for which $|v_{\text{syn}}(T) - v_{\text{meas}}|$ is minimal in each grid cell.

3.3. Joint Inversion of the Residual Gravity Field and Topography Using an Initial Seismic Tomography Model

The inversion procedure employs minimization of the residual mantle gravity anomalies and residual topography constrained by the initial density model of the upper mantle based on seismic tomography. Both fields are induced by density variations in the mantle, but their amplitudes have distinct dependencies on depth and size of the density anomalies (Kaban et al., 2015). Therefore, inversion of both fields provides a better resolution of the 3-D structure that would not be possible if a single physical parameter (the residual gravity or residual topography) were interpreted. The objective function, which should be minimized, is defined as the following (Kaban et al., 2015):

$$\min\left\{\|A\rho - g_{\text{res}}\|^2 + k\|B\rho - t_{\text{res}}\|^2 + \alpha\|\rho - \rho_{\text{ini}}\|^2\right\}, \tag{3}$$

where A and B are the integral operators converting densities to gravitational and topographic perturbations, respectively, $k = 2\pi G\rho$ is the factor normalizing topography with respect to gravity, and the third term represents a regularization condition, which requires that the final density variations should be close to the initial model or shall be minimized if such a model is not available ($\rho_{\text{ini}} = 0$). This is an Occam-type inversion, and the strength of stabilization of the solution is controlled by the damping factor α.

The inversion is done in the spherical harmonic domain, where it can be made separately for each degree/order set of the coefficients, which significantly reduces computational problems. In this way, it is also possible to take into account dynamic effects in the viscous mantle with the use of a "kernel" technique (e.g., Forte & Peltier, 1991). This approach requires a global distribution of all parameters; therefore, the models of Antarctica have been embedded in the global ones as described below. The impact of mantle density variations is estimated by taking into account dynamic effects, for which purposes we use a predefined radial viscosity distribution, which is based on mineral physics constraints and geodynamic models (Steinberger & Calderwood, 2006). Viscosity variations in the upper mantle can be significant, especially between EANT and WANT. The potential effect of plausible viscosity changes on the inversion results has been tested (e.g., Kaban et al., 2015, supporting information), and it has been demonstrated that it is relatively insignificant since topography kernels for long wavelengths are close to 1 in the uppermost mantle. Additionally, this effect has been evaluated with the code ProSpher (Petrunin, Kaban, et al., 2013), which can cope with high lateral viscosity variations.

Density variations are determined for seven layers starting from the depth of 15 km and down to 300 km (from 50 to 300 km with a step of 50 km). The density best represents the middle point of each layer. The bottom of the model should be below the deepest lithospheric keels (<240 km, e.g., Kuge & Fukao, 2005), which are the main target of the present study. The uppermost layer with the central depth of 15 km is included to account for two possible uncertainties: (1) the crustal density and (2) the Moho depth in WANT and offshore, where it is relatively shallow. As well, we assume that the inverted densities for the

50-km layer can be partially related to Moho uncertainties in EANT. A joint inversion of the residual topography and gravity provides the ability to locate depth of density anomalies; therefore, starting from the depth of 100 km, the calculated density variations are insignificantly influenced by the crustal uncertainties (Kaban et al., 2015). The relative damping factor α has been chosen based on numerical tests and corresponds to the point in which the calculated density perturbations start to increase rapidly while decreasing α. The results show only a small effect when the damping factor is changed by a factor of 2 in either direction from this point (Kaban et al., 2015).

Numerical tests showed that the method successively reproduces density variations. This method works even when density anomalies are not present in the initial model, as demonstrated by numerical tests (Kaban et al., 2015) and in the study of Asia and Western Pacific for the subduction zone beneath the Ryukyu and Marianna arcs, which is not resolved by the initial tomography model (Kaban et al., 2016b). However, in this case the amplitude of density variations might be reduced by up to 30–40% due to damping. Additional details and numerical tests that prove reliability of the inversion method can be found in Kaban et al. (2015).

3.4. Update of the Compositional Model

In the previous step, the inversion of residual gravity and residual topography yields density variations caused by compositional variations. In cratonic EANT, we assume that these variations are caused by depletion in heavy elements (iron), hence increasing the magnesium number Mg #. For quantification, we follow Tesauro et al., 2014, and calculate the density change that compensates a 0.1 increase in Mg # $\Delta\rho = -0.0016$ g/cm^3. Using this factor, we calculate the new Mg # in every grid point. In order to determine the new mineral fractions, we assume a linear variation between the two end-member compositions defined in section 3.2 in both mineral fractions and magnesium number Mg # of the bulk rock and pick the mineral fractions associated with the new Mg #. The minimal change in depletion is defined as a 0.1 increase in Mg #. Smaller density decreases, or positive values, are not compensated, and thus, the initial primitive composition assumed remains unchanged.

4. Initial Data

4.1. Tomography Models

The seismic velocity structure of Antarctica has been imaged using surface wave tomography at both global (SL2013sv; Schaeffer & Lebedev, 2013) and regional (AN1-S; An et al., 2015b) scales. For the SL2013sv data set, a total of three-fourth million broadband seismograms at a period range of 11–450 s were analyzed to create a global triangular grid with roughly 280-km horizontal spacing for 14 layers of depths between 56 and 720 km. Several resolution tests were conducted, and for Antarctica, columnar perturbations of ±300 m/s with a width of 6.6° were well resolved at 80-km depth. At 260-km depth, these features could still be resolved but showed some smearing. Beneath Antarctica, the model mainly shows the division of the continent into the two regions, EANT and WANT, but also shows some local reduction of S wave velocity, such as that observed around the Gamburtsev Subglacial Mountains (Figure 3b), and maximum velocities along the eastern flank of the TAM and in central Dronning Maud Land. The general division is also clearly visible in the AN1-S model (Figure 3a), but small scale variations as well as amplitudes vary notably in comparison. At 100-km depth, amplitudes for the SL2013sv model vary between $v_s = 4.73$ km/s in EANT and $v_s = 4.15$ km/s in WANT. While the maximum value in EANT, located at the Lambert Graben, is similar for the AN1-S model ($v_s = 4.78$ km/s), velocities in WANT are much lower and reach anomalous minimal values of $v_s = 3.94$ km/s. For this model, which only covers Antarctica, a total of 10,000 Rayleigh wave fundamental-mode dispersion curves registered at 122 broadband seismic stations were used to create a grid with horizontal spacing of 120 km and 51 depth layers. The thickness of these layers varies from 2.5 km down to a depth of 20 km and a thickness of 25 km between 250 km and the maximum depth of 325 km. The horizontal resolution length varies with direction and depth between 150 km in 50-km depth and 500 km in 200-km depth for continental Antarctica. In this study, both tomography models are converted to temperature, allowing a better distinction between valid structures and artifacts caused by the inversion process.
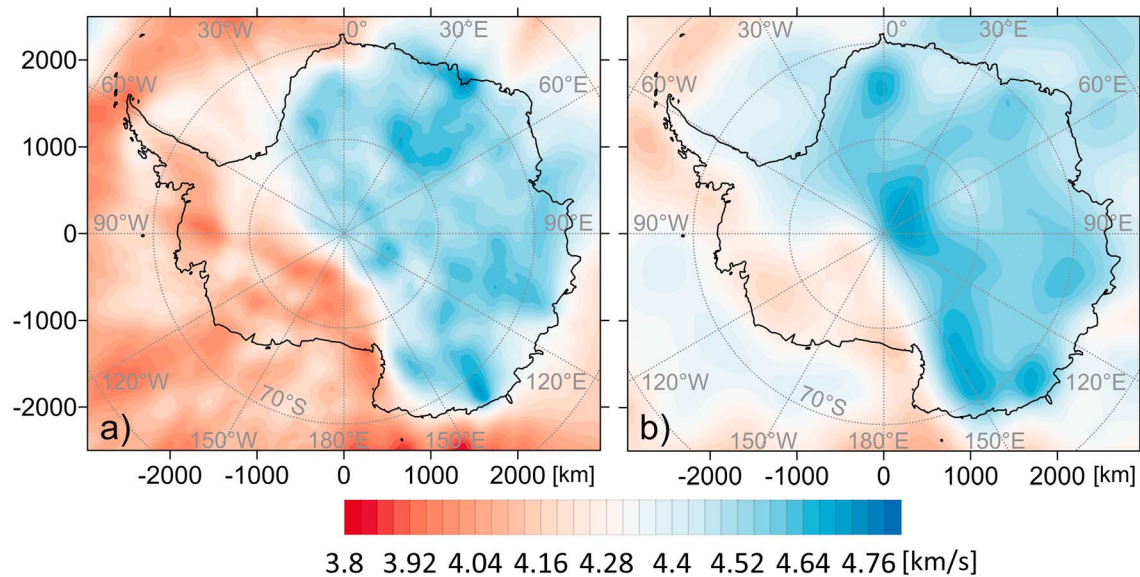
AGU
100
ADVANCING EARTH
AND SPACE SCIENCE

Geochemistry, Geophysics, Geosystems

10.1029/2018GC008033

Figure 3. Horizontal cross sections through the seismic velocity models of (a) AN1-S (An et al., 2015b) and (b) SL2013sv (Schaeffer & Lebedev, 2013) at a depth of 100 km.

4.2. Model of the Crust

The lateral density variations in the Earth's crust induce very strong gravity variations that may mask upper mantle effects. Therefore, it is crucial to remove this crustal effect from the observed gravity field. The Moho discontinuity is an interface with one of the strongest density contrast within the lithosphere (Rabbel et al., 2013). Hence, accurate knowledge of the depth of this discontinuity is most important when modeling gravity fields. Existing Moho maps in Antarctica either contain large gaps in coverage (e.g., AN1 Moho; An et al., 2015b; Baranov & Morelli, 2013), are not well constrained seismically, or exhibit nonnegligible deviations from seismic measurements of Moho depths (e.g., AN1 Crust; An et al., 2015b; Laske & Masters, 2013). Therefore, we combine existing models to create a new and improved map of Moho depths for the Antarctic continent.

We built this new map using a compilation of all existing Moho depths from receiver function, reflection, and refraction measurements (AN1 Moho, An et al., 2015b; Janik et al., 2014; Lamarque et al., 2015; circles in Figure 4a). Interpolation is carried out within a 150-km radius around these data points applying a remove-compute-restore technique suggested by Stolk et al. (2013). Large gaps remain especially in EANT in Dronning Maud Land and between 90° and 150°E. These gaps are filled in with the AN1-Crust model from seismic surface wave tomography (An et al., 2015b). The resulting final Moho map (Figure 4a) shows the distinction between EANT and WANT with a minimum in the West Antarctic Rift System, while the Transantarctic Mountains are characterized by shallow to intermediate Moho. The deepest Moho can be found around the Gamburtsev Subglacial Mountains and in northern Dronning Maud Land.

In order to determine the mantle gravity field, the effect of the crust has to be removed from the observed gravity field. To date, no density model of the crystalline crust exists for Antarctica on a continental scale. Therefore, we create a new, first-order model of lateral density variation within the crust. We start by calculating the depth-average crustal S wave velocity using the AN1-S (An et al., 2015b) model from the bedrock topography down to the Moho depth as determined in the previous step. Subsequently, we compile v_p/v_s ratios measured over Antarctica (Bayer et al., 2009; Finotello et al., 2011; Kanao & Shibutani, 2012; Kumar et al., 2014; Miyamachi et al., 2003) and calculate an average value of $\langle v_p/v_s \rangle_{av} = 1.77$ for the Antarctic continent to convert from average crustal v_s to v_p. In the final step, we employ the nonlinear conversion method by Christensen and Mooney (1995) to obtain crustal density from the lateral P wave velocity variation. Density perturbations were computed relative to a 1-D reference model, which is the same as that employed in previous studies for North America, Eurasia, and Middle East (Kaban et al., 2014, 2016a, 2016b). The results are shown in Figure 4b.
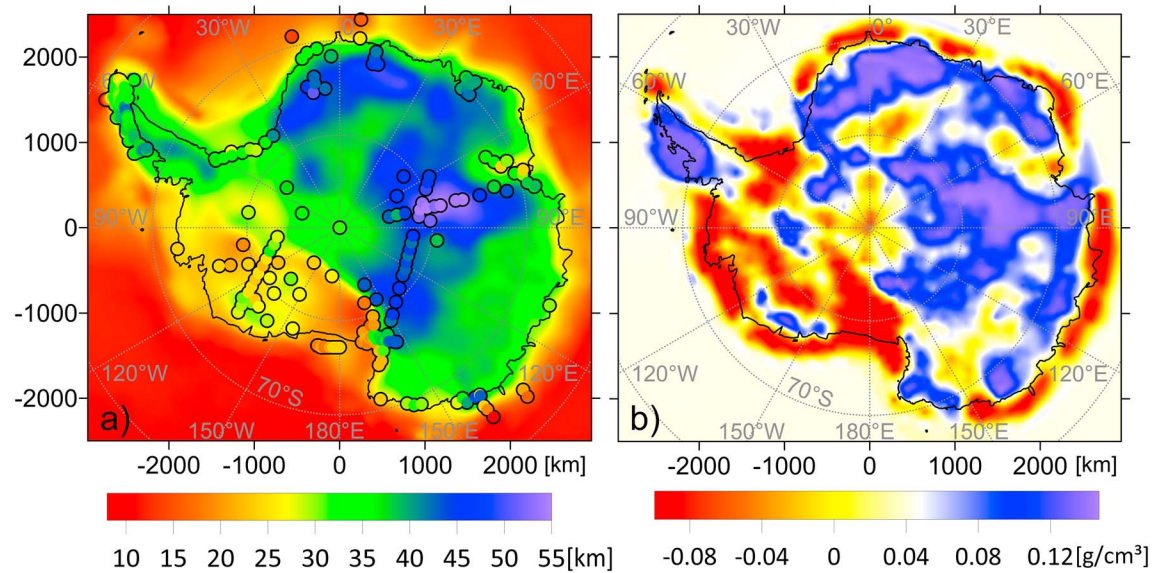
Figure 4. (a) Map of the Moho depth with superimposed determinations from refraction, reflection, and receiver function data (circles) (An et al., 2015b; Janik et al., 2014; Lamarque et al., 2015). (b) Average density perturbations of the crystalline crust.

It should be noted that the constructed crustal model is just a first approximation and is used as a starting point to reduce the ambiguity of the inverse problem. As described above, the inversion scheme includes the option to correct for its uncertainties.

4.3. Gravity Model

The initial gravity data set is a combination of the Eigen-6c4 (Förste et al., 2014) and the AntGG (Scheinert et al., 2016) model (Figure 5a). The former combines terrestrial and satellite data from GRACE, GOCE, and LAGEOS with a maximum resolution of 2,190 spherical harmonics degree and order. The actual resolution varies regionally and depends chiefly on the incorporated terrestrial data, thus limiting it to around 200 km in Antarctica for this model. The latter is a compilation of ground-based, shipborne, and airborne gravity anomaly measurements and includes 13 million data points, covering 73% of the Antarctic continent at 10 km resolution. It adds new and improved short wavelength structures to the Eigen-6c4 data set but is biased on longer wavelengths because of large gaps especially over EANT. Therefore, for our initial free air gravity model, the Eigen-6c4 data are used for wavelengths of $\lambda > 250$ km and the AntGG data for $\lambda < 150$ km with a gradual transition for 150 km $< \lambda <$ 250 km. As it was mentioned above, maximal horizontal resolution of the employed crustal model is about 110–150 km; therefore, the ground observations only marginally improve the satellite based model.

In order to obtain the residual mantle gravity field, we subsequently removed the effects of topography, water and ice columns, density variations in the crust, and Moho variations (Figure 5b). The anomalous effect of these layers was computed relative to the same 1-D reference model as used in section 4.2. This makes it possible to directly compare the results obtained for different continents. The reference model consists of two layers (0–15 km with the density of 2.7 g/cm^3 and 15–40 km of 2.94 g/cm^3), underlain by the upper mantle with the density of 3.35 g/m^3. Although this model is continental, it is isostatically balanced with the normal oceanic lithosphere of 180 Ma age (Kaban & Schwintzer, 2001). Therefore, the total gravity effect of all crustal layers down to the Moho will be the same when employing both reference models (oceanic and continental), as demonstrated by a smooth transition from the continental to the oceanic part (Figure 5b). Basically, plausible changes of the 1-D reference model only lead to a constant shift of the computed residual anomalies (Mooney & Kaban, 2010), which is not considered in this study.

The effect of each layer has been computed using a 3-D scheme on a spherical Earth as a sum of all tesseroids limited by geographical coordinates (in this case 1° × 1°) and upper/lower boundaries of the layer. A detailed description of this technique can be found in Kaban et al. (2016a). It has been demonstrated before (e.g.,
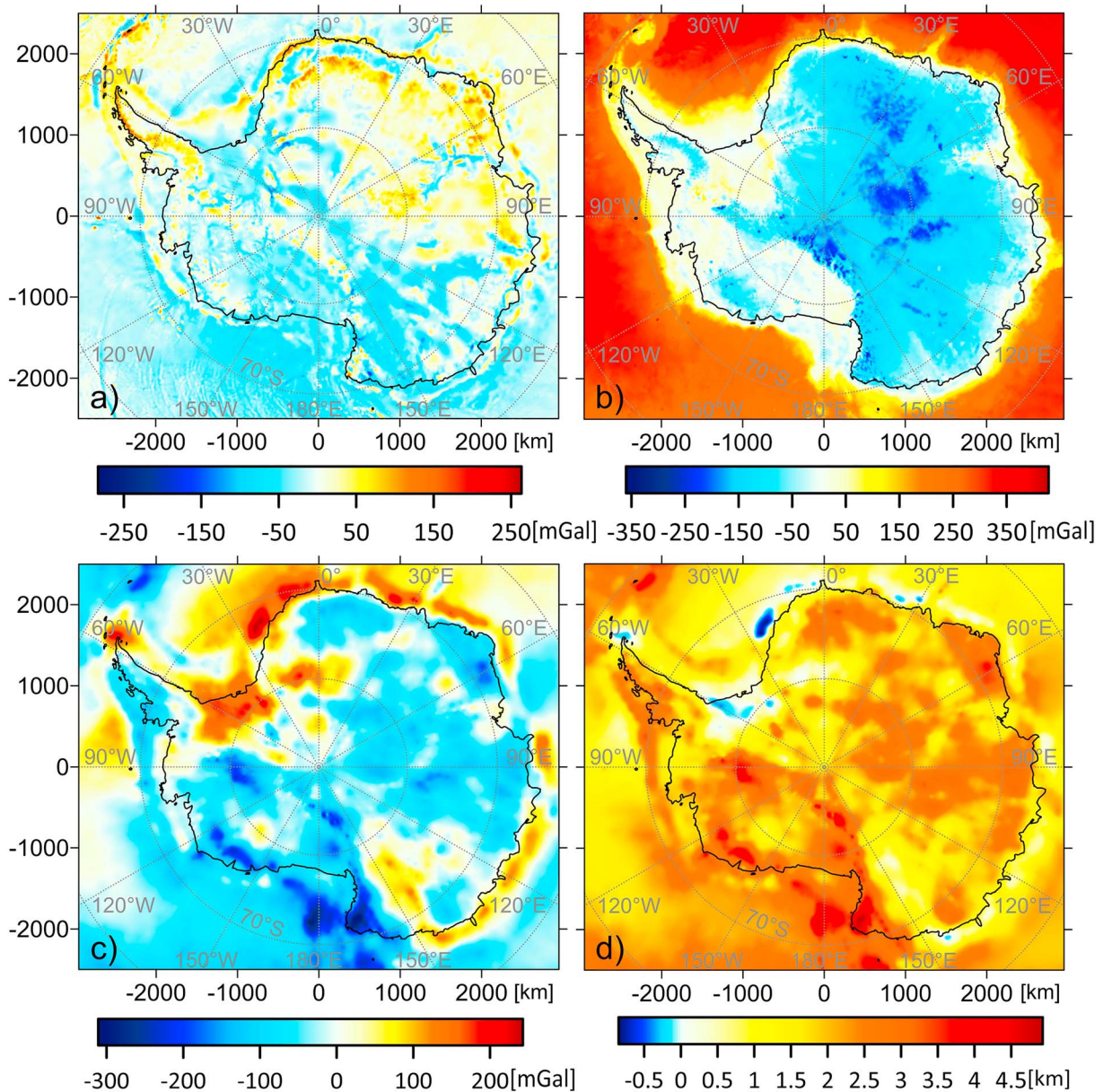
Figure 5. (a) Free air gravity anomalies and (b) Bouguer gravity anomalies. (c) Residual mantle gravity anomalies obtained after removal of the crustal gravity effects and the effect of deep density heterogeneities (below 325 km) from the observed data. (d) Residual topography calculated for a reference density of 2.67 g/cm^3. Zero level corresponds to the reference density model.

Kaban et al., 2004) that the effect of distant zones may produce very significant trends over continental-wide structures. Therefore, when calculating the effects of each crustal layer, we consider its variations for the whole Earth. Also, the inversion scheme based on spherical harmonic decomposition requires global coverage for all parameters. For these purposes, the crustal model of Antarctica has been embedded into a global one in the same way as it was previously done for North America (Kaban et al., 2014) and for Asia (Kaban et al., 2016b). For these purposes, we used the Crust1.0 model (Laske & Masters, 2013), which was improved in several regions (chiefly Eurasia, Australia, and North America) based on recent studies. Although the global model is not well defined in many regions, this is not important for remote areas since they produce only regional trends in limited areas comparable to Antarctica (Kaban et al., 2004).

Information on surface elevation, bedrock topography, and ice thickness are provided by Bedmap2 (Fretwell et al., 2013), bathymetry south of 60°S by RTopo-2 (Schaffer et al., 2014). We calculate the gravity effect of

each load according to Kaban et al. (2016a). The densities used in these calculations are $\rho_w = 1.03$ g/cm^3 for the water column and $\rho_t = 2.67$ g/cm^3 as the reference density for the upper crust. For the ice column, we chose a constant average density of $\rho_i = 0.92$ g/cm^3 according to Chen et al. (2017). Subsequently, we subtract the gravity effect caused by lateral variations in Moho depth, which causes the most significant changes and the gravity effect caused by the density variations within the crust as observed in our crustal model. The corrections for the residual topography are calculated analogously. In addition, we remove the effect of deep mantle density heterogeneities below 325 km based on global dynamic models (Kaban et al., 2015). The effect of the glacial-isostatic adjustment can also affect the residual gravity anomaly. To remove it, we employed a long-wavelength part of the isostatic anomalies calculated by Kaban et al. (2004). In Antarctica these anomalies clearly show a minimum associated with the noncompensated depression after partial deglaciation. The residual gravity field and residual topography are shown in Figures 5c and 5d. These anomalies are negatively correlated since the original density anomalies oppositely affect the residual gravity and residual topography. For example, any positive density anomaly produces an increase of the gravity field while the effect on the residual topography is negative since it sinks the whole lithospheric column downward.

Mooney and Kaban (2010) discuss in detail the potential errors of the residual mantle gravity anomalies and residual topography. They concluded that in areas well covered by seismic determinations the total uncertainty combining all factors is about 40 mGal for the gravity field and 0.35 km for the residual topography. In areas with poor seismic coverage, these uncertainties increase to about 75 mGal and 0.65 km, correspondingly (Mooney & Kaban, 2010). However, these estimates cannot be directly used for Antarctica. First of all, we do not have a reliable model of the thickness and density of the subglacial sediments, which effect may amount to −100 mGal or even more. Second, uncertainties of the receiver function and tomography results, which are largely used in the crustal model of Antarctica, are not defined and likely exceed the uncertainties of models derived from seismic refraction and reflection profiles, data that form the basis for crustal models in other continents. Therefore, we consider the initial crustal model as an approximation, and this model will be improved in the inversion of the residual fields.

Generally, the amplitudes of the residual mantle gravity anomalies are not significant over Antarctica compared to other continents such as North America (Kaban et al., 2014) and Eurasia (Kaban et al., 2016b) and are dominated by medium to low negative anomalies (−100 to −170 mGal). Only limited areas in WANT show stronger anomalies than in north Victoria Land (<−300mGal). In EANT, negative gravity features have lower amplitudes (up to −170mGal) and are limited to the area between 30°E and 120°E and to northern Dronning Maud Land. This demonstrates that generally composition and temperature induced density variations are well balanced considering their integral effect through the depth. In contrast, southern Dronning Maud Land is characterized by very high gravity variations (up to 190 mGal), as well as the adjacent Filchner-Ronne Ice-shelf (up to 250 mGal). The last region of high gravity variation with values reaching 130 mGal is located in the Wilkes Subglacial Basin. The ring of high gravity values around the shores of EANT is likely related to the transition from continental to oceanic lithosphere. It can also be related to insufficient resolution of the crustal model; in particular, a sharp decrease of the Moho depth and an increase of the crustal density off the border of Antarctica would reduce these positive anomalies.

5. Results

5.1. Temperature

The initial temperature distribution closely reflects the input velocity models. We calculate temperatures for depth slices between 50 and 300 km to obtain two independent thermal models with a spacing of 50 km. Representative depth slices for 100, 150, and 200 km are shown in Figure 6. In the first iteration based on a uniform primitive composition, both the SL2013 (Figures 6a–6c) and the AN1-S (Figures 6g and 6h) models show a clear distinction between EANT and WANT with temperatures generally over 1,100 °C in WANT at a depth of 100 km for SL2013 and over 1200 °C for AN1-S with maximum values of approximately 1,330 and 1,400 °C, respectively. Both models attribute significantly lower temperatures to EANT yet show strong differences in small scale structures and amplitudes. During the iterative process, compositional variations are determined within EANT, and their influence on the temperature model is calculated. Convergence is reached in the third iteration, and the resulting temperature distributions are shown in Figures 6d–6f for
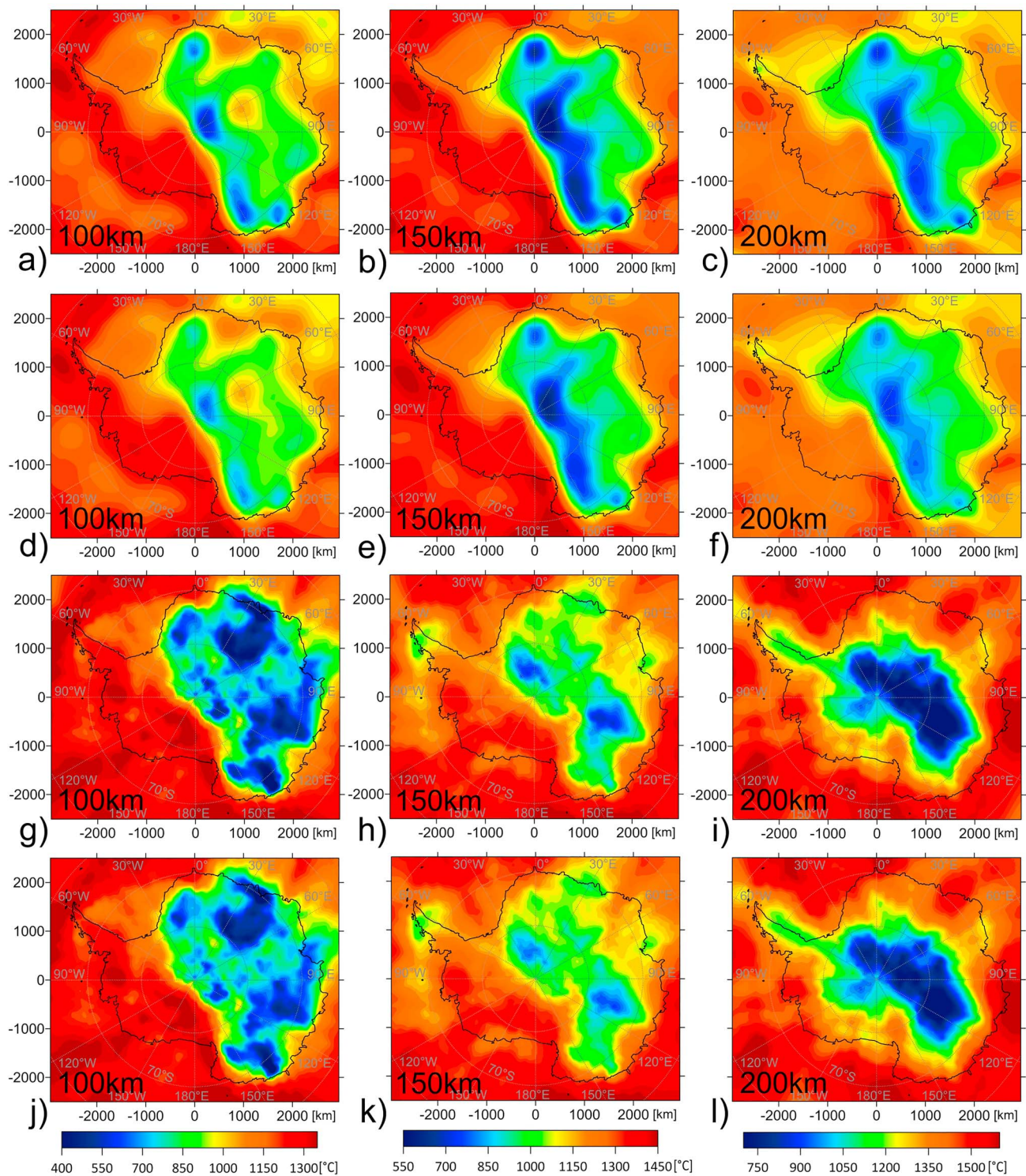
Figure 6. Temperature variations estimated for 100 (first column), 150 (second column), and 200 km (third column). Panels (a)–(f) are estimated on the basis of the SL2013 model, with panels (a)–(c) representing results from the first iteration and (d)–(f) representing the third and final iteration. Panels (g)–(l) are based on the AN1-S model in the first (panels (g)–(i)) and final (panels (j)–(l)) iteration.

the SL2013 and Figures 6j–6l for the An1-S model. For both models, adding compositional variations does not change the size and distribution of anomalies but elevates temperatures in depleted areas by up to 150 °C. From here on out, we will only examine the models calculated in the final iteration.

In the temperature model derived from SL2013, the majority of EANT is characterized by temperatures below 900 °C for depths of 100 and 150 km. The coldest zones can be found around the South Pole with values below 610 °C, in central Dronning Maud Land (780 °C), and along the eastern flank of the Transantarctic Mountains (690 °C) for the same depths. The TAM themselves are characterized by a transition from very high temperatures (around 1,300 °C at 100 km) in the west to those aforementioned low temperatures in the east in all depth layers under investigation. A local maximum of 1,050 °C is present around the Gamburtsev Subglacial Mountains. At depths of 200 km and below, the temperatures are generally higher and the anomalies smoother, but the general division of the continent is still present and the lithospheric root extends to a depth of roughly 250 km in EANT.

In comparison, the model based on AN1-S is generally characterized by lower temperatures with most of EANT not exceeding 800 °C at 100-km depth. Anomalously low temperatures (<300 °C) are located in the Wilkes Subglacial Basin and inland and offshore Enderby Land. The Aurora Subglacial Basin exhibits temperatures below 500 °C. Like in the SL2013 model, we find local minima just east of the South Pole and in Dronning Maud Land, but those anomalies are shifted in comparison and show more fragmentation. At 150- and 200-km depth, the cold structures are shifted more and more toward central Antarctica with the strongest anomalies in the Aurora Subglacial Basin around the South Pole with anomalous values below 600 °C at 200 km. Additionally, temperatures in the western Transantarctic Mountains even decrease with increasing depth (1,200 °C at 100 km and 940 °C at 200 km), which is probably caused by a strong local increase in velocity in the tomography model that cannot be explained by pressure increase due to depth alone.

When estimating uncertainties in the conversion of seismic velocities to temperatures, several factors have to be taken into account that might vary on a regional scale (Kaban et al., 2014). The choice of the compositional model can cause errors in temperature as high as 200 °C in the presence of high depletion (Lee, 2003). An error in S wave velocity of 0.05 km/s in the input model will cause temperature variations of up to 150 °C in cold cratons (Tesauro et al., 2012). In hot areas, the effect of this uncertainty is diminished, while the effects due to the uncertainties in anelasticity increase. The uncertainties of the elastic parameters are dominated by those of the temperature derivatives, translating into errors in temperature of 70 °C above 300 km (Tesauro et al., 2010). At temperatures over 900 °C, the uncertainty in the attenuation model can also cause errors of about 100 °C in the final model (Jackson et al., 2002). Conversely, our analysis clearly demonstrated that a choice of the tomography model is much more critical for estimation of mantle temperatures than the uncertainty due to the conversion from seismic velocities to temperatures.

5.2. Density

We jointly invert the residual gravity field and the residual topography to obtain the 3-D density distribution of the Antarctic upper mantle. Gravity field variations are more sensitive to changes in composition and depletion while seismic velocities exhibit stronger dependencies to temperature. Iteratively combining these results with the seismic tomography with the gravity based estimates allows to distinguish between temperature-induced versus composition-induced density changes. The abovementioned inversion has been conducted for seven depth layers: in addition to the six depth slices already discussed for temperature variations, the uppermost layer centered at 15 km contains errors within the assumed crustal model. The layer centered at 50 km also includes potential corrections of the initial Moho model. Same as for temperature variations, representative horizontal slices at depths of 100, 150, and 200 km are shown in Figure 7 for the SL2013 model and in Figure 8 for the AN1-S model. For the former, two vertical cross sections are displayed in Figure 9.

Figures 7a–7c and 8a–8c depict the density changes caused by temperature variation for the SL2013 and the AN1-S model, respectively. The thermal density variation resembles closely the temperature variations obtained in the previous step with low temperatures causing high densities and vice versa. For 100 km, the thermal density variation ranges from −0.034 to 0.029 g/cm^3 and from −0.038 to 0.085 g/cm^3 for the SL2013 and AN1-S models, respectively. For the former, the maximum offset of extreme values decreases
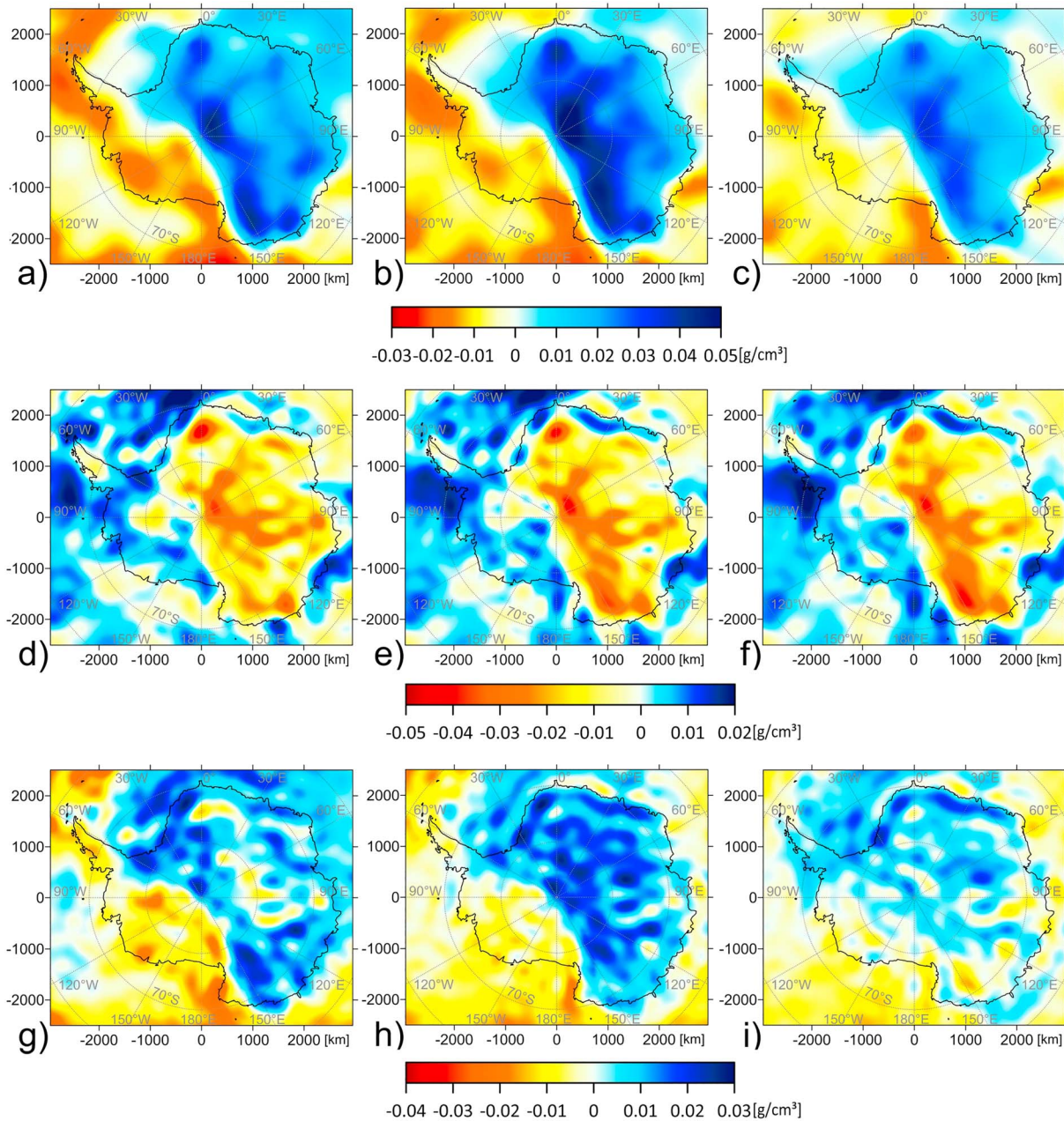
Figure 7. Density variations estimated for 100 (first column), 150 (second column), and 200 km (third column) based on the SL2013 tomography model. Panels (a)–(c) show thermal, (d)–(f) compositional, and (g)–(i) total density variations as obtained in the final iteration.

monotonously with increasing depth to −0.016 to 0.025 g/cm^3 in 200 km, while the latter exhibits minimal values for 150 km (−0.031–0.044 g/cm^3) and a subsequent increase to −0.035 to 0.061 g/cm^3 in 200 km.

Just like the temperature and thermal density variations, composition-induced density variations (Figures 7d–7f and Figures 8d–8f) show a clear division between EANT with lower and WANT with higher densities. The values lie relatively constant for different depths and models between −0.048 ± 0.005 and 0.025 ± 0.002 g/cm^3, but local structures of anomalies differ between the two models. If corrections derived from SL2013 are used in the inversion process, the lowest densities are found in Dronning Maud Land and along the eastern flank of the Transantarctic Mountains. With corrections from AN1-S, the minimum in Dronning Maud Land still exists but is significantly weaker in comparison and further weakens with depth. The minimum along the flanks of the TAM is shifted further toward central EANT with the lowest values in
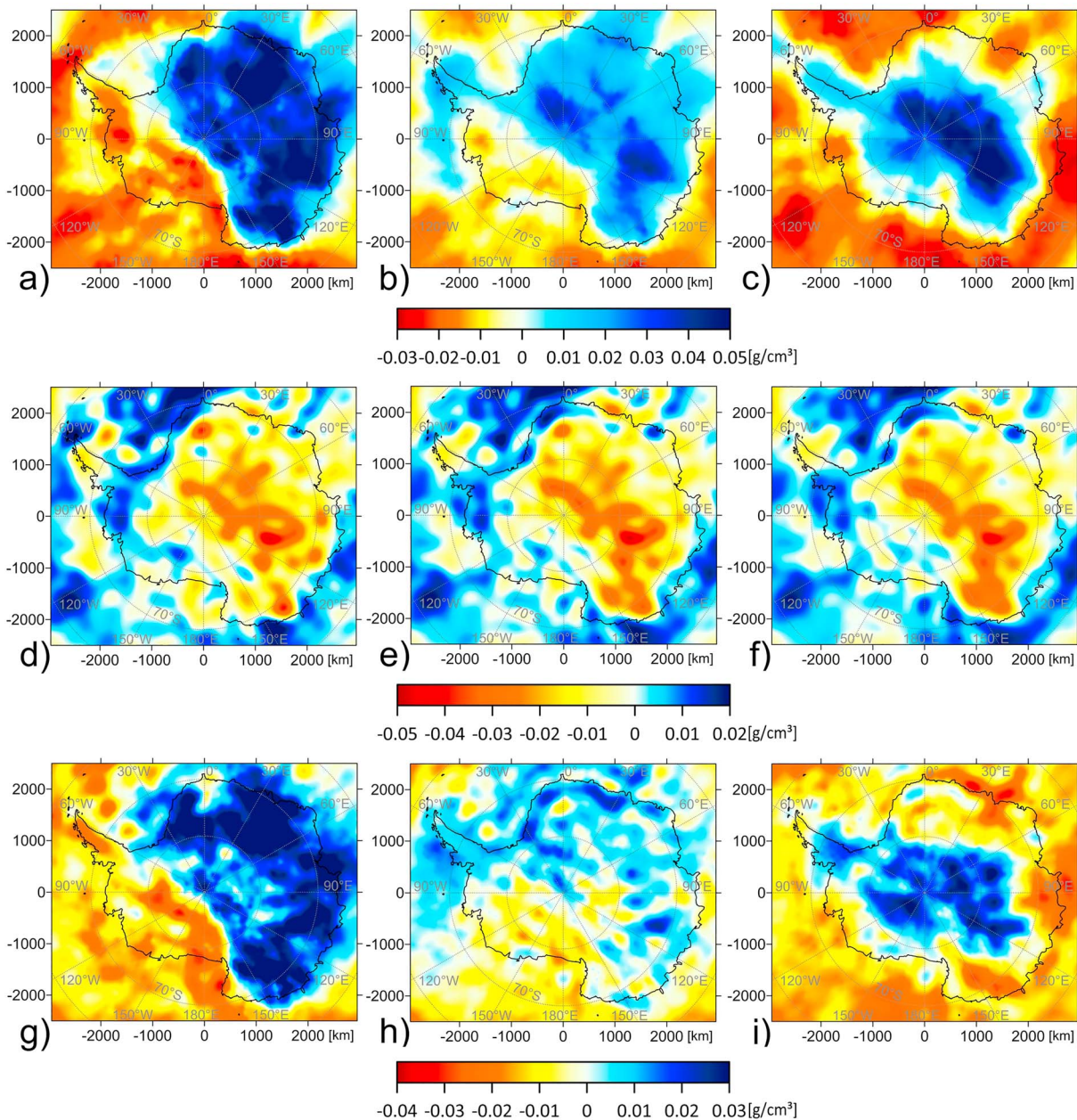
Figure 8. Density variations estimated for 100 (first column), 150 (second column), and 200 km (third column) based on the AN1-S tomography model. Panels (a)–(c) show thermal, (d)–(f) compositional, and (g)–(i) total density variations as obtained in the final iteration.

the Aurora Subglacial Basin. Variations on smaller scales are likely artifacts caused by the conversion into spherical harmonics during the inversion process and are dependent on the maximum degree and order used in the process. To limit the occurrence of artifacts but still retain a reasonable resolution, a maximum value of 120 degree and order was chosen.

Adding up both fields yields the total density variation within Antarctica (Figures 7g–7i and Figures 8g–8i). In the first model, the density distribution in 100-km depth spanning between −0.034 and 0.029 g/cm³ resemble closely that of the residual gravity and the residual topography, indicating that density variations located in the uppermost mantle control these fields to a large extent. The distinction between EANT and WANT is reflected in the total density variations, as well, but is fading when density contrasts decrease at 200 km (−0.016–0.025 g/cm³) and beyond. Over the majority of Antarctica, thermal density variations
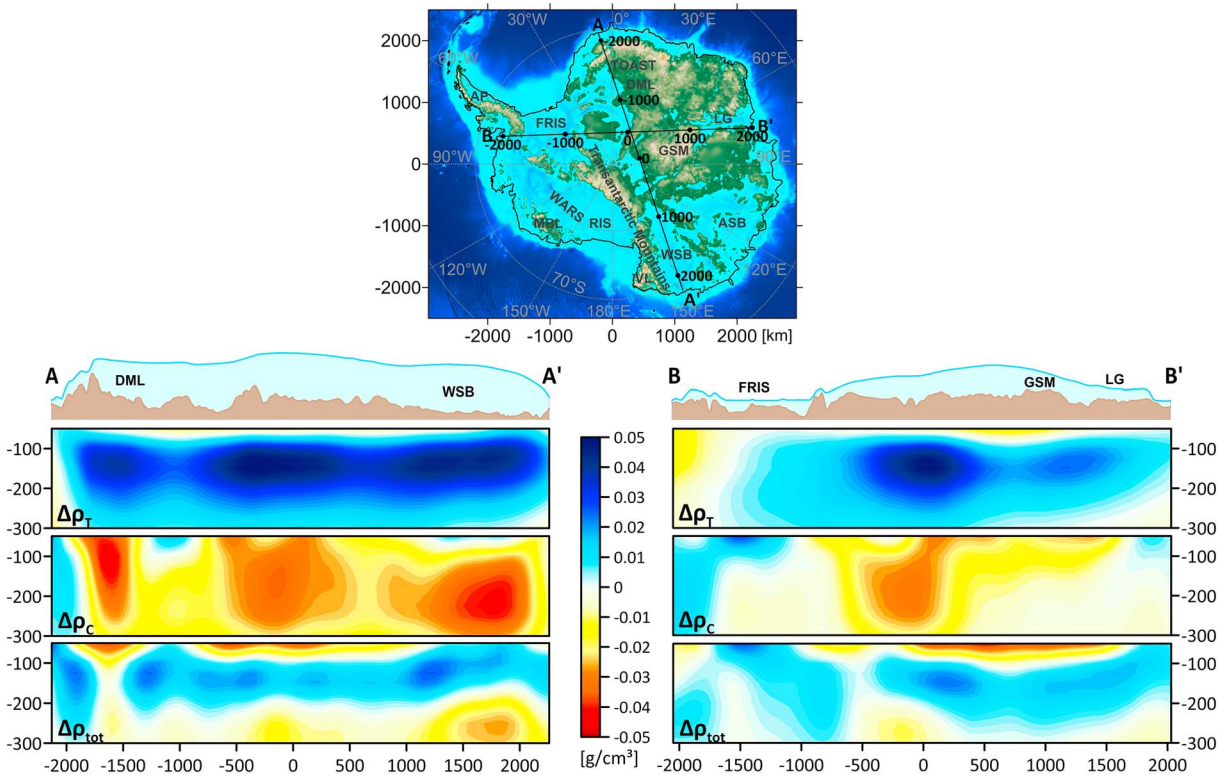
Figure 9. Bedrock topography (top) with location of two cross sections through the density variations calculated based on the SL2013sv model. First row = surface (blue) and bedrock (brown) topography, second row = thermal density variations, third row = compositional density variation, fourth row = total density variations, WSB = Wilkes Subglacial Basin; DML = Dronning Maud Land; GSM = Gamburtsev Subglacial Mountains; FRIS = Filchner-Ronne Ice Shelf; LG = Lambert Graben.

dominate in the total field, causing generally high density in EANT and low density in WANT. Only the strong minima in compositional density in Dronning Maud Land and close to the Pole are clearly reflected in the total field at a depth of 100 km. The model based on AN1-S is also strongly dominated by thermal density variations, especially at 100 (-0.037–0.067 g/cm^3) and 200 km (-0.036–0.38 g/cm^3) where anomalously low temperatures and hence high thermal density variations are estimated. A clear distinction between EANT and WANT is only visible at 100-km depth.

The cross sections (Figure 9) give a better idea about the depth extents of both thermal and compositional density variations. Within EANT, high thermal density features (> 0.026 g/cm^3) extend to depths between 200 and 250 km, while no such structures are visible for WANT, indicating significantly lower depth of the lithospheric root (<100 km). The roots of the (low) compositional density structures in EANT reach even deeper and are still visible below 250 km in Dronning Maud Land, central Antarctica, and in the Wilkes Subglacial Basin.

5.3. Composition

During the iterative process, we calculate not only temperature and density variations but also changes in composition in terms of Mg # for cratonic EANT. The resulting depletion variations for the above introduced representative depth slices are shown in Figure 10 based on the SL2013 model (panels a–c) and on the AN1-S model (panels d–f). The former exhibits strongest depletion in central Dronning Maud Land with up to Mg # = 92 in 100-km depth with another local maximum around the South Pole (Mg # = 91.3). Another highly depleted area can be found along the eastern flank of the Transantarctic Mountains with Mg # = 91.6 at 200 km. The Lambert Graben and Gamburtsev Subglacial Mountains as well as the Aurora Subglacial Basin on the other hand exhibit low to no depletion and preserve almost primitive mantle composition. These structures become increasingly clear with increasing depth. The model based on AN1-S shows similar yet weaker structures in Dronning Maud Land and around the South Pole. Maximum depletion can be found
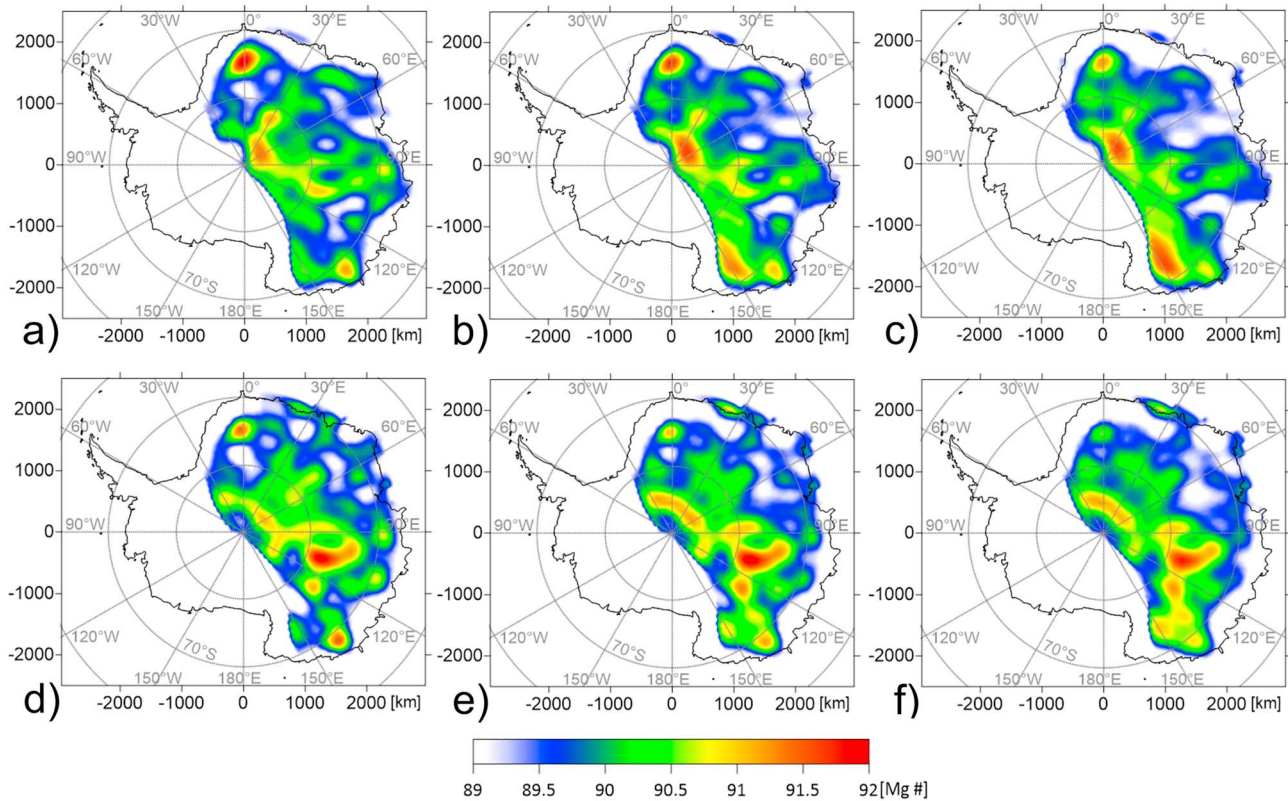
Figure 10. Depletion variations in terms of Mg # ($100 \times$ Mg/(Mg + Fe)) estimated for 100 (first column), 150 (second column), and 200 km (third column) based on the SL2013 tomography model (panels (a)–(c)) and on AN1-S model (panels (d)–(f)) as obtained in the final iteration.

in the central Aurora Subglacial Basin (Mg # = 91.9), though. In the vicinity of the Lambert Graben, an almost undepleted area is present but seems to be less distinct and shifted further toward Enderby Land in comparison with the SL2013 model. In contrast to the SL2013sv model, no such minimum exists around the Aurora Subglacial Basin.

6. Discussion

The joint inversion of gravity and tomography data allows us to get new insight into the lithospheric structures of Antarctica. The choice of the seismic tomography model used in the inversion strongly affects the results obtained in the iterative scheme. Both tomographic models used in this study stem from surface wave tomography but yield quite different amplitudes and local structures, likely caused by different data and inversion techniques. Especially at 200 km and below, the AN1-S model exhibits very high velocities in EANT, translating into temperatures that are far below the temperatures estimated for comparable cratonic regions derived from xenolith data (e.g., Griffin et al., 2004; Hasterok & Chapman, 2011), and can explain the differences with the model SL2013sv. In some regions like the western TAM, temperatures estimated using the AN1-S model even decrease with increasing depth. Furthermore, it causes the total density variations to be strongly dominated by thermal variations possibly masking compositional changes. Therefore, we conclude that the AN1-S model is not well suited for our study and the discussion will be focused on the analysis of the results obtained using the SL2013sv model.

WANT is characterized by very low variations in compositional density ($<\pm 0.015$ g/cm^3), indicating that the negative variations in residual gravity are chiefly induced by a hot upper mantle present in this region. In EANT, however, the negative residual density anomalies can no longer be explained by thermal variations alone. Here negative compositional density variations are necessary to explain the gravity observations, indicating high depletion in iron. Positive compositional density variations without equivalent expression in seismic velocity present in WANT can be explained by the presence of eclogite, which can cause an

increase of the density from 3.3 to up to 3.5 g/cm^3 (e.g., Kurtz & Garland, 1976) while being seismically indistinguishable from peridotite. This hypothesis has been suggested by Tesauro et al. (2014) to explain the positive anomalies in the off-cratonic areas and is supported by petrological studies that found eclogite originated from the Ross orogeny in Northern Victoria Land (Godard & Palmeri, 2013, and Melchiorre et al., 2011), corresponding very well with the local maximum in compositional density in our study. Similar conditions can be argued for other continental sutures within WANT, yet no xenolith data exist in these regions to date due to poor exposure. EANT and WANT also differ strongly in lithospheric thickness. While WANT is characterized by lithospheric thickness well below 100 km, the thermal lithospheric root in EANT reaches values of >200 km.

Within EANT, several regions are characterized by both low temperatures and strongly negative compositional density variations, namely along the eastern flank of the Transantarctic Mountains with the strongest anomalies in the Wilkes Subglacial Basin and close to the South Pole and in central Dronning Maud Land, indicating the presence of Archean to Paleoproterozoic cratonic blocs. The Mawson craton located in Wilkes Land (Boger, 2011; Leitchenkov et al., 2016) is of such Archean to Paleoproterozoic origin and coincides well with the anomaly in the Wilkes Subglacial Basin. Based on xenolith data from the Miller Range, Boger (2011) further suggests a continuation of the Mawson Craton into EANT with a distinct fragment of Archean to Paleoproterozoic basement around the Nimrod Group, coinciding with the second abovementioned anomaly. Dronning Maud Land is a region of key importance when studying the formation and subsequent break-up of Gondwana as it played a central role in this process. Recent studies (e.g., Jacobs et al., 2015, 2017; Ruppel et al., 2018) found evidence that large parts of this region are characterized by juvenile early Mesoproterozoic to Neoproterozoic terranes that form part of the Tonian Oceanic Arc Super Terrane. These authors also suggest the presence of an unidentified terrane or craton. Since we find a structure with low temperature, negative compositional density, and high depletion there, we argue that this unidentified terrane is of Precambrian age. In these regions, compositional density variations also suggest a much deeper lithospheric root of over 250 km.

The Lambert Graben is characterized by low compositional density variation (<±0.01 g/cm^3), low to no depletion in terms of Fe, and slightly elevated temperatures at shallow depth compared to its surroundings. Hence, rejuvenation of the lithospheric mantle must have taken place during the rifting process in this failed rift system. Two distinct phases of denudation have been suggested for the Lambert Graben (e.g., Lisker et al., 2003), one in the late Paleozoic coincident with the onset of rifting and one in the Cretaceous, that could account for such rejuvenation. The Aurora Subglacial Basin is characterized by similar conditions in the models based on SL2013sv but contains the strongest differences to the models based on AN1-S, which found negative compositional density anomalies and high depletion in its southernmost part. Boger (2011) interprets this region to be of Mesoproterozoic age. Additionally, the region is characterized by several large suture zones with the Indo-Australo-Antarctic Suture and the Aurora Fault being the largest and lying directly within the region of low depletion. They both represent tectonic boundaries that played a major role in the assembly and break-up of supercontinent Rodinia in Proterozoic times (Aitken et al., 2014, 2016). Paleozoic to Mesozoic reactivation possibly linked to the rifting activity in the East Antarctic Rift System (Aitken et al., 2014; Cianfarra & Maggi, 2017; Ferraccioli et al., 2011) may have caused further rejuvenation of this terrane, hence, supporting the results obtained using the SL2013sv model.

7. Conclusion

We combine gravity and seismic tomography data in an iterative inversion scheme to create a 3-D model of the Antarctic lithosphere that quantifies temperature, density, and compositional variations. The residual gravity and topography models were estimated using a new model of lateral density variations within the crust and an improved map of Moho depth variation, both created in this study. Temperature variations were calculated using a regional (AN1-S) and a global (SL2013sv) tomography model. We conclude that the choice of tomography model has a significant role when estimating lithospheric temperatures. Anomalously low velocities in WANT as well as anomalously high velocities in cratonic EANT at 200 km and below when using the AN1-S model leading to unrealistic temperature variations indicate a preference to the results obtained using SL2013sv for interpretation. Incorporating compositional changes into the temperature calculations raised the final temperatures by up to 150 °C.

A clear distinction between EANT and WANT is visible in all parameters that have been investigated in this study. In WANT, the lithospheric root is very shallow (<100 km), and density variations predominantly stem from high upper mantle temperatures. Existing positive compositional density variations, for example, in Northern Victoria Land, are argued to be caused by the presence of eclogite. In EANT, both thermal and compositional density variations suggest a much deeper lithospheric root (>200 km). Furthermore, temperature variations alone are not sufficient to explain the residual gravity and topography variations and negative compositional density variations caused by high depletion in iron are required.

Several key regions in EANT are characterized by negative, compositional-induced density variations, indicating high depletion in iron and low temperatures. In Dronning Maud Land, recent studies (e.g., Jacobs et al., 2015, 2017) infer that the rejuvenated Tonian Oceanic Arc Super Terrane was terminated against an unidentified, possibly cratonic fragment that coincides well with one of the abovementioned regions ($T < 800$ °C, $\rho < -0.045$ g/cm^3, Mg # = 92), thus supporting their interpretation. The Mawson Craton in the Wilkes Subglacial Basin is characterized by similar conditions ($T < 650$ °C, $\rho < -0.041$ g/cm^3, Mg # = 91.6) and could possibly be linked to a low temperature and high depletion zone (also likely of cratonic origin) close to the South Pole ($T < 550$ °C, $\rho < -0.04$ g/cm^3, Mg # = 91.6).

Undepleted lithosphere is located in the Lambert Graben and in the Aurora Subglacial Basin. The former is a part of the East Antarctic Rift System (Ferraccioli et al., 2011), and its rejuvenation likely took place during the rifting process that might be as recent as the Cretaceous (Lisker et al., 2003). The process of rifting could be linked to the reactivation of the Indo-Australo-Antarctic Suture and the Aurora Fault, two major suture zones within the Aurora Subglacial Basin, thus explaining the low depletion as being due to the rejuvenation of the lithosphere in this region.

References

Aitken, A. R. A., Betts, P. G., Young, D. A., Blankenship, D. D., Roberts, J. L., & Siegert, M. J. (2016). The Australo-Antarctic Columbia to Gondwana transition. *Gondwana Research*, *29*(1), 136–152. https://doi.org/10.1016/J.GR.2014.10.019

Aitken, A. R. A., Young, D. A., Ferraccioli, F., Betts, P. G., Greenbaum, J. S., Richter, T. G., et al. (2014). The subglacial geology of Wilkes Land, East Antarctica. *Geophysical Research Letters*, *41*, 2390–2400. https://doi.org/10.1002/2014GL059405

An, M., Wiens, D. A., Zhao, Y., Feng, M., Nyblade, A., Kanao, M., et al. (2015a). Temperature, lithosphere-asthenosphere boundary, and heat flux beneath the Antarctic Plate inferred from seismic velocities. *Journal of Geophysical Research: Solid Earth*, *120*, 8720–8742. https://doi.org/10.1002/2015JB011917

An, M., Wiens, D. A., Zhao, Y., Feng, M., Nyblade, A. A., Kanao, M., et al. (2015b). *S*-velocity model and inferred Moho topography beneath the Antarctic Plate from Rayleigh waves. *Journal of Geophysical Research: Solid Earth*, *120*, 359–383. https://doi.org/10.1002/2014JB011332

Baranov, A., & Morelli, A. (2013). The Moho depth map of the Antarctica region. *Tectonophysics*, *609*, 299–313. https://doi.org/10.1016/j.tecto.2012.12.023

Bayer, B., Geissler, W. H., Eckstaller, A., & Jokat, W. (2009). Seismic imaging of the crust beneath Dronning Maud Land, East Antarctica. *Geophysical Journal International*, *178*(2), 860–876. https://doi.org/10.1111/j.1365-246X.2009.04196.x

Behrendt, J. C. (1999). Crustal and lithospheric structure of the West Antarctic Rift System from geophysical investigations—A review. *Global and Planetary Change*, *23*(1–4), 25–44. https://doi.org/10.1016/S0921-8181(99)00049-1

Boger, S. D. (2011). Antarctica—Before and after Gondwana. *Gondwana Research*, *19*(2), 335–371. https://doi.org/10.1016/j.gr.2010.09.003

Burton-Johnson, A., Halpin, J. A., Whittaker, J. M., Graham, F. S., & Watson, S. J. (2017). A new heat flux model for the Antarctic Peninsula incorporating spatially variable upper crustal radiogenic heat production. *Geophysical Research Letters*, *44*, 5436–5446. https://doi.org/10.1002/2017GL073596

Cammarano, F., Goes, S., Vacher, P., & Giardini, D. (2003). Inferring upper-mantle temperatures from seismic velocities. *Physics of the Earth and Planetary Interiors*, *138*(3–4), 197–222. https://doi.org/10.1016/S0031-9201(03)00156-0

Chen, B., Haeger, C., Kaban, M. K., & Petrunin, A. G. (2017). Variations of the effective elastic thickness reveal tectonic fragmentation of the Antarctic lithosphere. *Tectonophysics*, *746*, 412–424. https://doi.org/10.1016/j.tecto.2017.06.012

Christensen, N. I., & Mooney, W. D. (1995). Seismic velocity structure and composition of the continental crust: A global view. *Journal of Geophysical Research*, *100*(B6), 9761–9788. https://doi.org/10.1029/95JB00259

Cianfarra, P., & Maggi, M. (2017). Cenozoic extension along the reactivated Aurora Fault System in the East Antarctic Craton. *Tectonophysics*, *703-704*, 135–143. https://doi.org/10.1016/j.tecto.2017.02.019

Dalziel, I. W. D., & Elliot, D. H. (1982). West Antarctica: Problem child of Gondwanaland. *Tectonics*, *1*(1), 3–19. https://doi.org/10.1029/TC001i001p00003

Danesi, S., & Morelli, A. (2001). Structure of the upper mantle under the Antarctic Plate from surface wave tomography. *Geophysical Research Letters*, *28*(23), 4395–4398. https://doi.org/10.1029/2001GL013431

Deschamps, F., Trampert, J., & Snieder, R. (2002). Anomalies of temperature and iron in the uppermost mantle inferred from gravity data and tomographic models. *Physics of the Earth and Planetary Interiors*, *129*(3-4), 245–264. https://doi.org/10.1016/S0031-9201(01)00294-1

Ebbing, J., Pappa, F., Ferraccioli, F., van der Wal, W., & Barletta, V. R. (2016). Deciphering the changes in the lithospheric structure of antarctica by combining seismological and satellite gravity gradient data. *AGU Fall Meeting Abstracts*.

Ferraccioli, F., Bell, R. E., Blankenship, D. D., Young, D. A., Eagles, G., Forsberg, R., et al. (2016). Revealing the crustal architecture of the least understood composite craton on Earth: East Antarctica. *AGU Fall Meeting Abstracts*.

Ferraccioli, F., Finn, C. a., Jordan, T., Bell, R. E., Anderson, L., & Damaske, S. (2011). East Antarctic rifting triggers uplift of the Gamburtsev Mountains. *Nature*, *479*(7373), 388–392. https://doi.org/10.1038/nature10566

Finotello, M., Nyblade, A., Julia, J., Wiens, D., & Anandakrishnan, S. (2011). Crustal V_p-V_s ratios and thickness for Ross Island and the Transantarctic Mountain front, Antarctica. *Geophysical Journal International*, *185*(1), 85–92. https://doi.org/10.1111/j.1365-246X.2011.04946.x

Förste, C., Bruinsma, S., Abrikosov, O., Flechtner, F., Marty, J.-C., Lemoine, J.-M., et al. (2014). EIGEN-6C4—The latest combined global gravity field model including GOCE data up to degree and order 1949 of GFZ Potsdam and GRGS Toulouse. *EGU General Assembly*, *16*, 3707. https://doi.org/https://doi.org/10.5880/icgem.2015.1

Forte, A. M., & Peltier, R. (1991). Viscous flow models of global geophysical observables: 1. Forward problems. *Journal of Geophysical Research*, *96*(B12), 20,131–20,159. https://doi.org/10.1029/91JB01709

Fretwell, P., Pritchard, H. D., Vaughan, D. G., Bamber, J. L., Barrand, N. E., Bell, R., et al. (2013). Bedmap2: Improved ice bed, surface and thickness datasets for Antarctica. *The Cryosphere*, *7*(1), 375–393. https://doi.org/10.5194/tc-7-375-2013

Godard, G., & Palmeri, R. (2013). High-pressure metamorphism in Antarctica from the Proterozoic to the Cenozoic: A review and geodynamic implications. *Gondwana Research*, *23*(3), 844–864. https://doi.org/10.1016/J.GR.2012.07.012

Godey, S., Deschamps, F., Trampert, J., & Snieder, R. (2004). Thermal and compositional anomalies beneath the North American continent. *Journal of Geophysical Research*, *109*, B01308. https://doi.org/10.1029/2002JB002263

Goodge, J. W. (2018). Crustal heat production and estimate of terrestrial heat flow in central East Antarctica, with implications for thermal input to the East Antarctic ice sheet. *The Cryosphere*, *12*(2), 491–504. https://doi.org/10.5194/tc-12-491-2018

Griffin, W. L., O'Reilly, S. Y., Doyle, B. J., Pearson, N. J., Coopersmith, H., Kivi, K., et al. (2004). Lithosphere mapping beneath the North American plate. *Lithos*, *77*(1-4), 873–922. https://doi.org/10.1016/j.lithos.2004.03.034

Harrowfield, M., Holdgate, G. R., Wilson, C. J. L., & McLoughlin, S. (2005). Tectonic significance of the Lambert graben, East Antarctica: Reconstructing the Gondwanan rift. *Geology*, *33*(3), 197–200. https://doi.org/10.1130/G21081.1

Hasterok, D., & Chapman, D. S. (2011). Heat production and geotherms for the continental lithosphere. *Earth and Planetary Science Letters*, *307*(1–2), 59–70. https://doi.org/10.1016/j.epsl.2011.04.034

Hole, M. J., & LeMasurier, W. E. (1994). Tectonic controls on the geochemical composition of Cenozoic, mafic alkaline volcanic rocks from West Antarctica. *Contributions to Mineralogy and Petrology*, *117*(2), 187–202. https://doi.org/10.1007/BF00286842

Huerta, A. D., & Harry, D. L. (2007). The transition from diffuse to focused extension: Modeled evolution of the West Antarctic rift system. *Earth and Planetary Science Letters*, *255*(1–2), 133–147. https://doi.org/10.1016/j.epsl.2006.12.011

Jackson, I., Fitz Gerald, J. D., Faul, U. H., & Tan, B. H. (2002). Grain-size-sensitive seismic wave attenuation in polycrystalline olivine. *Journal of Geophysical Research*, *107*(B12), 2360. https://doi.org/10.1029/2001JB001225

Jacobs, J., Elburg, M., Läufer, A., Kleinhanns, I. C., Henjes-Kunst, F., Estrada, S., et al. (2015). Two distinct Late Mesoproterozoic/Early Neoproterozoic basement provinces in central/eastern Dronning Maud Land, East Antarctica: The missing link, 15–21°E. *Precambrian Research*, *265*, 249–272. https://doi.org/10.1016/j.precamres.2015.05.003

Jacobs, J., Opås, B., Elburg, M. A., Läufer, A., Estrada, S., Ksienzyk, A. K., et al. (2017). Cryptic sub-ice geology revealed by a U-Pb zircon study of glacial till in Dronning Maud Land, East Antarctica. *Precambrian Research*, *294*, 1–14. https://doi.org/10.1016/j.precamres.2017.03.012

Janik, T., Grad, M., Guterch, A., & Środa, P. (2014). The deep seismic structure of the Earth's crust along the Antarctic Peninsula—A summary of the results from Polish geodynamical expeditions. *Global and Planetary Change*, *123*, 213–222. https://doi.org/10.1016/j.gloplacha.2014.08.018

Kaban, M. K., El Khrepy, S., & Al-Arifi, N. (2016a). Isostatic model and isostatic gravity anomalies of the Arabian Plate and surroundings. *Pure and Applied Geophysics*, *173*(4), 1211–1221. https://doi.org/10.1007/s00024-015-1164-0

Kaban, M. K., Mooney, W. D., & Petrunin, A. G. (2015). Cratonic root beneath North America shifted by basal drag from the convecting mantle. *Nature Geoscience*, *8*(10), 797–800. https://doi.org/10.1038/ngeo2525

Kaban, M. K., & Schwintzer, P. (2001). Oceanic upper mantle structure from experimental scaling of VS and density at different depths. *Geophysical Journal International*, *147*(1), 199–214. https://doi.org/10.1046/j.0956-540x.2001.01520.x

Kaban, M. K., Schwintzer, P., & Reigber, C. (2004). A new isostatic model of the lithosphere and gravity field. *Journal of Geodesy*, *78*(6), 368–385. https://doi.org/10.1007/s00190-004-0401-6

Kaban, M. K., Stolk, W., Tesauro, M., El Khrepy, S., Al-Arifi, N., Beekman, F., & Cloetingh, S. A. P. L. (2016b). 3D density model of the upper mantle of Asia based on inversion of gravity and seismic tomography data. *Geochemistry, Geophysics, Geosystems*, *17*, 4457–4477. https://doi.org/10.1002/2016GC006458

Kaban, M. K., Tesauro, M., Mooney, W. D., & Cloetingh, S. A. P. L. (2014). Density, temperature, and composition of the North American lithosphere—New insights from a joint analysis of seismic, gravity, and mineral physics data: 1. Density structure of the crust and upper mantle. *Geochemistry, Geophysics, Geosystems*, *15*, 4781–4807. https://doi.org/10.1002/2014GC005483

Kanao, M., & Shibutani, T. (2012). Shear wave velocity models beneath Antarctic margins inverted by genetic algorithm for teleseismic receiver functions. In M. Kanao (Ed.), *Seismic waves—Research and analysis* (pp. 237–252). InTech. https://doi.org/10.5772/32130

Khan, A., Zunino, A., & Deschamps, F. (2013). Upper mantle compositional variations and discontinuity topography imaged beneath Australia from Bayesian inversion of surface-wave phase velocities and thermochemical modeling. *Journal of Geophysical Research: Solid Earth*, *118*, 5285–5306. https://doi.org/10.1002/jgrb.50304

Kuge, K., & Fukao, Y. (2005). High-velocity lid of East Antarctica: Evidence of a depleted continental lithosphere. *Journal of Geophysical Research*, *110*, B06309. https://doi.org/10.1029/2004JB003382

Kumar, P., Talukdar, K., & Sen, M. K. (2014). Lithospheric structure below transantarctic mountain using receiver function analysis of TAMSEIS data. *Journal of the Geological Society of India*, *83*(5), 483–492. https://doi.org/10.1007/s12594-014-0075-5

Kurtz, R. D., & Garland, G. D. (1976). Magnetotelluric measurements in eastern Canada. *Geophysical Journal of the Royal Astronomical Society*, *45*(2), 321–347. https://doi.org/10.1111/j.1365-246X.1976.tb00329.x

Lamarque, G., Barruol, G., Fontaine, F. R., Bascou, J., & Menot, R.-P. (2015). Crustal and mantle structure beneath the Terre Adelie Craton, East Antarctica: Insights from receiver function and seismic anisotropy measurements. *Geophysical Journal International*, *200*(2), 807–821. https://doi.org/10.1093/gji/ggu430

Laske, G., & Masters, G. (2013). Update on CRUST 1. 0—A 1-degree global model of Earth's crust. *EGU General Assembly*, *15*, 2658. Retrieved from http://meetingorganizer.copernicus.org/EGU2013/EGU2013-2658.pdf

Lee, C.-T. A. (2003). Compositional variation of density and seismic velocities in natural peridotites at STP conditions: Implications for seismic imaging of compositional heterogeneities in the upper mantle. *Journal of Geophysical Research*, *108*(B9), 2441. https://doi.org/10.1029/2003JB002413

Leitchenkov, G. L., Antonov, A. V., Luneov, P. I., & Lipenkov, V. Y. (2016). Geology and environments of subglacial Lake Vostok. *Philosophical Transactions of the Royal Society A: Mathematical, Physical and Engineering Sciences*, *374*(2059), 20140302. https://doi.org/10.1098/rsta.2014.0302

Lisker, F., Brown, R., & Fabel, D. (2003). Denudational and thermal history along a transect across the Lambert Graben, northern Prince Charles Mountains, Antarctica, derived from apatite fission track thermochronology. *Tectonics*, *22*(5), 1055. https://doi.org/10.1029/2002TC001477

Maule, C. F., Purucker, M. E., Olsen, N., & Mosegaard, K. (2005). Heat flux anomalies in Antarctica revealed by satellite magnetic data. *Science*, *309*(5733), 464–467. https://doi.org/10.1126/science.1106888

Melchiorre, M., Coltorti, M., Bonadiman, C., Faccini, B., O'Reilly, S. Y., & Pearson, N. J. (2011). The role of eclogite in the rift-related metasomatism and Cenozoic magmatism of Northern Victoria Land, Antarctica. *Lithos*, *124*(3–4), 319–330. https://doi.org/10.1016/J.LITHOS.2010.11.012

Miyamachi, H., Toda, S., Matsushima, T., & Takada, M. (2003). Seismic refraction and wide-angle reflection exploration by JARE-43 on Mizuho Plateau, East Antarctica. *Polar Geoscience*, *16*, 1–21.

Mooney, W. D., & Kaban, M. K. (2010). The North American upper mantle: Density, composition, and evolution. *Journal of Geophysical Research*, *115*, B12424. https://doi.org/10.1029/2010JB000866

Morelli, A., & Danesi, S. (2004). Seismological imaging of the Antarctic continental lithosphere: A review. *Global and Planetary Change*, *42*(1-4), 155–165. https://doi.org/10.1016/j.gloplacha.2003.12.005

O'Donnell, J. P., & Nyblade, A. A. (2014). Antarctica's hypsometry and crustal thickness: Implications for the origin of anomalous topography in East Antarctica. *Earth and Planetary Science Letters*, *388*, 143–155. https://doi.org/10.1016/j.epsl.2013.11.051

Owada, M., Kamei, A., Horie, K., Shimura, T., Yuhara, M., Tsukada, K., et al. (2013). Magmatic history and evolution of continental lithosphere of the Sør Rondane Mountains, eastern Dronning Maud Land, East Antarctica. *Precambrian Research*, *234*, 63–84. https://doi.org/10.1016/j.precamres.2013.02.007

Pappa, F., Ebbing, J., Ferraccioli, F., van der Wal, W., & Blank, B. (2018). A 3D lithospheric model of Antarctica and its implications on mantle viscosity. In *EGU General Assembly Conference Abstracts* (Vol. 20, p. 4939).

Petrunin, A. G., Kaban, M. K., Rogozhina, I., & Trubitsyn, V. (2013). Revising the spectral method as applied to modeling mantle dynamics. *Geochemistry, Geophysics, Geosystems*, *14*, 3691–3702. https://doi.org/10.1002/ggge.20226

Petrunin, A. G., Rogozhina, I., Vaughan, A. P. M., Kukkonen, I. T., Kaban, M. K., Koulakov, I., & Thomas, M. (2013). Heat flux variations beneath central Greenland's ice due to anomalously thin lithosphere. *Nature Geoscience*, *6*(9), 746–750. https://doi.org/10.1038/ngeo1898

Powell, C. M., Roots, S. R., & Veevers, J. J. (1988). Pre-breakup continental extension in East Gondwanaland and the early opening of the eastern Indian Ocean. *Tectonophysics*, *155*(1–4), 261–283. https://doi.org/10.1016/0040-1951(88)90269-7

Rabbel, W., Kaban, M., & Tesauro, M. (2013). Contrasts of seismic velocity, density and strength across the Moho. *Tectonophysics*, *609*, 437–455. https://doi.org/10.1016/j.tecto.2013.06.020

Ruppel, A., Jacobs, J., Eagles, G., Läufer, A., & Jokat, W. (2018). New geophysical data from a key region in East Antarctica: Estimates for the spatial extent of the Tonian Oceanic Arc Super Terrane (TOAST). *Gondwana Research*, *59*(c), 97–107. https://doi.org/10.1016/j.gr.2018.02.019. https://doi.org/10.1016/j.gr.2018.02.019

Schaeffer, A. J., & Lebedev, S. (2013). Global shear speed structure of the upper mantle and transition zone. *Geophysical Journal International*, *194*(1), 417–449. https://doi.org/10.1093/gji/ggt095

Schaffer, J., Timmermann, R., Arndt, J. E., Steinhage, D., & Kanzow, T. (2014). RTopo-2: A global dataset of ice sheet topography, cavity geometry and ocean bathymetry to study ice-ocean interactions in Northeast Greenland. *REKLIM Conference "Our Climate - Our Future", Berlin, Germany, 6 October 2014–9 October 2014*. Retrieved from http://epic.awi.de/37733/#.WFFkhlNeaOA.mendeley

Scheinert, M., Ferraccioli, F., Schwabe, J., Bell, R., Studinger, M., Damaske, D., et al. (2016). New Antarctic gravity anomaly grid for enhanced geodetic and geophysical studies in Antarctica. *Geophysical Research Letters*, *43*, 600–610. https://doi.org/10.1002/2015GL067439

Shapiro, N. M., & Ritzwoller, M. H. (2004). Inferring surface heat flux distributions guided by a global seismic model: Particular application to Antarctica. *Earth and Planetary Science Letters*, *223*(1–2), 213–224. https://doi.org/10.1016/j.epsl.2004.04.011

Simmons, N. A., Forte, A. M., & Grand, S. P. (2009). Joint seismic, geodynamic and mineral physical constraints on three-dimensional mantle heterogeneity: Implications for the relative importance of thermal versus compositional heterogeneity. *Geophysical Journal International*, *177*(3), 1284–1304. https://doi.org/10.1111/j.1365-246X.2009.04133.x

Steinberger, B., & Calderwood, A. R. (2006). Models of large-scale viscous flow in the Earth's mantle with constraints from mineral physics and surface observations. *Geophysical Journal International*, *167*(3), 1461–1481. https://doi.org/10.1111/j.1365-246X.2006.03131.x

Stixrude, L., & Lithgow-Bertelloni, C. (2005). Thermodynamics of mantle minerals - I. Physical properties. *Geophysical Journal International*, *162*(2), 610–632. https://doi.org/10.1111/j.1365-246X.2005.02642.x

Stolk, W., Kaban, M., Beekman, F., Tesauro, M., Mooney, W. D., & Cloetingh, S. (2013). High resolution regional crustal models from irregularly distributed data: Application to Asia and adjacent areas. *Tectonophysics*, *602*, 55–68. https://doi.org/10.1016/j.tecto.2013.01.022

ten Brink, U., & Stern, T. (1992). Rift flank uplifts and hinterland basins—Comparison of the Transantarctic Mountains with the great escarpment of southern Africa. *Journal of Geophysical Research*, *97*(B1), 569–585. https://doi.org/10.1029/91JB02231

Tesauro, M., Audet, P., Kaban, M. K., Bürgmann, R., & Cloetingh, S. (2012). The effective elastic thickness of the continental lithosphere: Comparison between rheological and inverse approaches. *Geochemistry, Geophysics, Geosystems*, *13*, Q09001. https://doi.org/10.1029/2012GC004162

Tesauro, M., Kaban, M. K., & Cloetingh, S. A. P. L. (2010). Thermal and rheological model of the European lithosphere. In S. Cloetingh & J. Negendank (Eds.), *New frontiers in integrated solid earth sciences* (pp. 71–101). Dordrecht: Springer Netherlands. https://doi.org/10.1007/978-90-481-2737-5_3

Tesauro, M., Kaban, M. K., Mooney, W. D., & Cloetingh, S. A. P. L. (2014). Density, temperature, and composition of the North American lithosphere—New insights from a joint analysis of seismic, gravity, and mineral physics data: 2. Thermal and compositional model of the upper mantle. *Geochemistry, Geophysics, Geosystems*, *15*, 4808–4830. https://doi.org/10.1002/2014GC005484

van Wijk, J. W., Lawrence, J. F., & Driscoll, N. W. (2008). Formation of the Transantarctic Mountains related to extension of the West Antarctic Rift System. *Tectonophysics*, *458*(1–4), 117–126. https://doi.org/10.1016/j.tecto.2008.03.009

Veevers, J. J. (2007). Pan-Gondwanaland post-collisional extension marked by 650-500 Ma alkaline rocks and carbonatites and related detrital zircons: A review. *Earth-Science Reviews*, *83*(1-2), 1–2), 1–47. https://doi.org/10.1016/j.earscirev.2007.03.001